Article

Reactive Adsorption of Gaseous Anisole by MCM–41-Supported Sulfuric Acid

Dandan Zhao [1], Jinjin Qian [1], Yaxu Wang [1], Zichuan Ma [1,*] and Xiaolong Ma [2,*]

1 Hebei Key Laboratory of Inorganic Nano-Materials, College of Chemistry and Material Sciences, Hebei Normal University, Shijiazhuang 050024, China
2 School of Environmental Science and Engineering, Hebei University of Science and Technology, Shijiazhuang 050018, China
* Correspondence: mazc@hebtu.edu.cn (Z.M.); maxiaolong2410@hebust.edu.cn (X.M.); Tel.: +86-0311-80787400 (Z.M.)

Abstract: To achieve the efficient resource treatment of aromatic volatile organic compounds (VOCs) of high toxicity, this work chose anisole as a representative pollutant and investigated its removal by an MCM–41-supported sulfuric acid (SSA/MCM–41) adsorbent. The results indicate that the SSA/MCM–41 adsorbent exhibited a reactive temperature range of 110–140 °C, in which the anisole removal ratio (X_a) was greater than 95%. The collected breakthrough adsorption data fit the dose–response model. In the comprehensive analysis of the process conditions, reducing the flow rate enhanced the theoretical breakthrough time and adsorption capacity ($t_{B,th}$ and $Q_{B,th}$), while reducing the inlet concentration or raising the bed height resulted in a first increasing and then slightly decreasing trend in the $Q_{B,th}$. As a result, the highest $t_{B,th}$ and $Q_{B,th}$ were 73.82 min and 247.56 mg g^{-1}, respectively. The FTIR and ^{1}H/^{13}C NMR results demonstrate that the adsorbed products included both 4-methoxybenzenesulfonic acid and 1-methoxy-4-(4-methoxyphenyl)sulfonylbenzene. Accordingly, the mechanism of reactive adsorption was proposed. Meanwhile, the spent SSA/MCM–41 could be desorbed and regenerated for cyclic reuse. It is believed that the results obtained will assist in promoting the application of the novel gas–solid adsorption approach in VOC treatment.

Keywords: supported sulfuric acid; MCM–41; anisole; reactive adsorption; sulfonation

1. Introduction

Not only are volatile organic compounds (VOCs) considered important precursors of secondary organic aerosols and ground ozone, but some of them also can be toxic and pathogenic [1–6]. Aromatics are widely recognized as highly polluting molecules, the emission of which requires additional attention [7–9]. Therefore, the purification of aromatics is an important topic in the field of environmental chemistry and engineering [9].

Traditional VOC purification methods mainly include thermal combustion, catalytic oxidation, photocatalytic degradation, and biodegradation, etc. [3,10–13]. Although these purification methods can achieve excellent mineralization rates of VOCs, the resource utilization of the VOC molecules is often forgone [14,15]. To achieve efficient resource treatment of VOCs, a reactive adsorption approach was proposed in our previous studies in which supported sulfuric acid could be used as the adsorbent for removing aromatic hydrocarbons [16]. The removal performance and transformation products of target pollutants is most probably linked to their molecular structures. However, only the o–xylene results have been reported to date [17–19]. Supported adsorbents that have been tested include silica-supported sulfuric acid (SSSA) [16], synthetic silica-supported sulfuric acids (SSAI and SSAII) [19], and mesoporous MCM–41- and SBA–15-supported sulfuric acids (SSA/MCM–41 and SSA/SBA–15) [17]. Among these supported sulfuric acids, the SSA/MCM–41 adsorbent exhibited the best adsorption activity for o–xylene. Practically, MCM–41 materials are a promising support widely used in the preparation of various adsorbents and

catalysts due to their strong thermal stability, abundant meso-/micropores and high surface area [20–22]. Therefore, in this work, mesoporous MCM–41 was selected as the support for preparing a supported sulfuric acid adsorbent.

Belonging to one of the hazardous VOC groups, anisole (metoxybenzene) is an aromatic hydrocarbon that presents as a colorless liquid with an aromatic odor, is commercially produced as synthesized compounds, and is used as an important intermediate in the production of pharmaceuticals and fragrances [23]. Because the methoxyl group of anisole is slightly weaker than the methyl group of *o*–xylene in electron-donating ability, this work chose anisole as the target pollutant for research. The objectives were: (1) to evaluate the response of anisole to SSA/MCM–41 with a gradient-varying temperature; (2) to acquire adsorption data for the anisole/SSA/MCM–41 system from a series of constant-temperature breakthrough experiments and to theoretically fit those data to investigate anisole adsorption behavior; and (3) to analyze the adsorbed species to explore the process mechanism. We believe that the results obtained will assist in promoting the application of the novel gas–solid adsorption approach in VOC treatment.

2. Results and Discussion

2.1. Response of Anisole Removal to Temperature

As can be seen in Figure 1, the response curve of the anisole removal ratio (X_a) vs. temperature (*T)* presented an inverted U-shaped profile, indicating that there was an appropriate temperature window of 110–140 °C for the reactive adsorption of anisole by SSA/MCM–41, with both sides experiencing an activation stage (upward trend) and a deactivation stage (downward trend). The response curve of anisole on SSA/MCM–41 was similar to that of *o*–xylene on various supported sulfuric acid systems such as SSA/MCM–41, SSA/SBA–15, SSA/SG, and silica sulfuric acid [16–19]. Therefore, anisole was expected to follow the same reactive adsorption mechanism as *o*–xylene, i.e., it was removed from the gaseous stream by the sulfonation reaction with the anchored H_2SO_4 molecules on SSA/MCM–41.
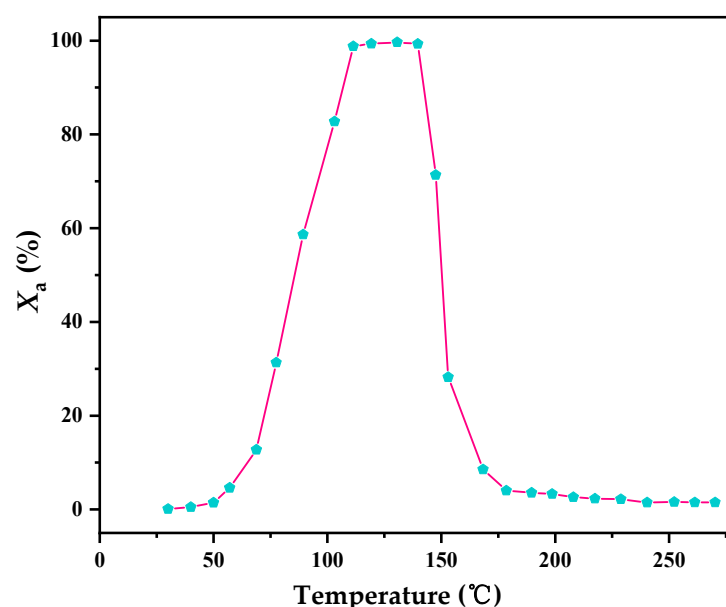

Figure 1. Plots of anisole removal ratios (X_a) vs. temperature (*T*).

Under the same conditions of C_{in} = 6.4 mg L^{-1}, *h* = 14.3 mm, and *v* = 50 mL min^{-1}, the experimental dot plots and their dose–response model fitting curves corresponding to different temperatures (110, 120, 130 and 140 °C) were used to quantitatively analyze the effect of temperature on the anisole removal performance, as depicted in Figure 2 and Table 1. Each of the four S-shaped breakthrough curves can be divided into three stages to show the anisole decay dissimilarity: the early stage exhibited stable and high

removal ratios ($X_a \geq 95\%$), the intermediate stage exhibited rapidly decaying adsorption ($5\% < X_a < 95\%$), and the late stage exhibited inefficient adsorption ($X_a \leq 5\%$). This behavior is similar to conventional physisorption or chemisorption in gas–solid systems [24–26]; thus, these dynamic reactive adsorption data could be well described by the dose–response model ($R^2 > 0.99$) [27–29]. The theoretical metrics $t_{B,th}$ and $Q_{B,th}$ calculated by this model were both very close to the corresponding experimental values. Thus, the $t_{B,th}$ and $Q_{B,th}$ metrics were used to contrastively analyze the anisole removal performance. It can also be seen in Figure 2 that with the increase in temperature, the intermediate stage of these curves moved first to the right and then to the left, searching out an optimum temperature of 130 °C. In this experiment, the values of $t_{B,th}$ and $Q_{B,th}$ corresponding to 130 °C were 34.39 min and 222.06 mg·g^{-1}, respectively.
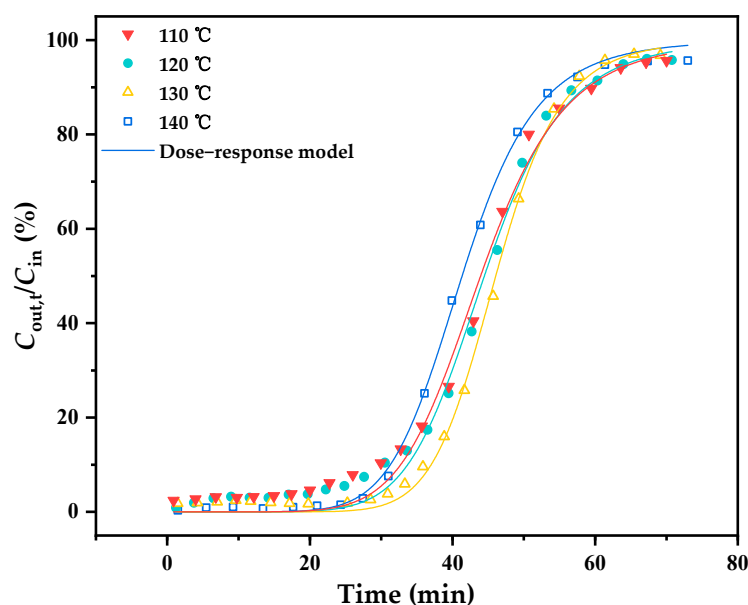
Figure 2. Experimental breakthrough dot plots and the dose–response model fitting curves at different temperatures.

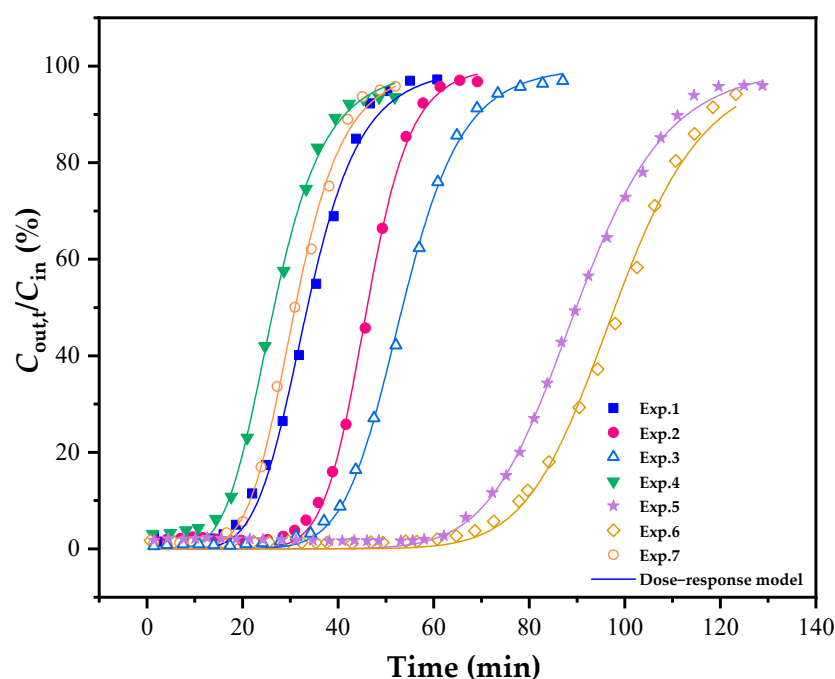**Table 1.** Adsorption metrics and model parameters of anisole at different temperatures.

Parameters and Metrics	Temperature (°C)			
	110	**120**	**130**	**140**
Experimental:				
t_B (min)	20.90	23.60	32.20	28.99
Q_B (mg g^{-1})	129.51	146.50	201.93	183.30
Dose–response model:				
q_0 (mg g^{-1})	0.28	0.28	0.29	0.26
a	7.46	7.68	10.03	7.88
R^2	0.9912	0.9928	0.9977	0.9989
$t_{B,th}$ (min)	28.28	30.32	34.39	28.49
$Q_{B,th}$ (mg g^{-1})	192.22	199.12	222.06	183.91

2.2. Comprehensive Analysis of the Effects of the Process Conditions

At the optimum temperature of 130 °C, the dynamic adsorption tests for anisole flowing through the SSA/MCM–41–filled bed under different process conditions (Table 2) were employed to investigate the effects of the inlet concentration (C_{in}), bed height (h), and gas flow rate (v) on the anisole removal performance. The experimental dot plots and the corresponding dose–response model fitting curves obtained from the seven experiments are shown in Figure 3. The theoretical metrics are listed in Table 3. The main findings were as follows.

Table 2. Summary of the experimental conditions.

Exp. No.	Inlet Concentration (mg L^{-1})	Bed Height (mm)	Flow Rate (mL min^{-1})
1 (■)	8.8	14.3	50
2 (●)	6.4	14.3	50
3 (△)	4.0	14.3	50
4 (▼)	6.4	10.5	50
5 (★)	6.4	20.0	50
6 (◇)	6.4	14.3	25
7 (○)	6.4	14.3	75

Figure 3. Experimental breakthrough dot plots and dose–response model fitting curves for the seven experiments.

Table 3. Adsorption performance metrics of anisole under different conditions.

Metrics	Exp. No.						
	1	2	3	4	5	6	7
$t_{B,th}$ (min)	20.53	34.39	37.69	14.69	66.12	73.82	19.1
$Q_{B,th}$ (mg g^{-1})	189.92	222.06	152.98	189.62	215.80	247.56	184.45

(1) All the breakthrough curves exhibited a typical S–shape with a three characteristic stages attributable to the occurrence of the sulfonation reaction between the anisole molecules and the SSA/MCM–41 surface.

(2) Under the stable conditions of v = 50 mL min^{-1} and h = 14.3 mm, when C_{in} is successively reduced (Exp. No. 1, 2, and 3), the curves moved significantly towards the right-hand side; furthermore, the $t_{B,th}$ greatly extended, while the $Q_{B,th}$ values increased first and then decreased slightly, implying that the reactive adsorption process of anisole was affected by both the diffusion driving force and the surface reaction rate [30].

(3) When C_{in} and h were constant and v reduced from 75 mL min^{-1} to 25 mL min^{-1} (Exp. No. 7, 2, and 6), a significant rightward shift of the curves occurred. Correspondingly,

both $t_{B,th}$ and $Q_{B,th}$ monotonically increased, which also demonstrates the importance of the residence time for the anisole adsorption.

(4) Comparing the results from the above seven experiments, it was found that the highest values of $t_{B,th}$ (73.82 min) and $Q_{B,th}$ (247.56 mg g^{-1}) were both obtained in Exp. No. 6, and that the corresponding optimal process details were 6.4 mg L^{-1} of C_{in}, 14.3 mm of h, 25 mL min^{-1} of v, and 130 °C of T.

2.3. Analysis of the Adsorbed Products and the Removal Mechanism of Anisole

Figure S1 shows the SEM images and EDS results of the spent SSA/MCM–41 before (a, b) or after (c, d) desorption. Obviously, before desorption, the appearance of the sample was rough with attached agglomerated particles, and the four elements C, O, Si, and S were detected. However, after desorption, the surface of the sample was smooth, and only the two elements O and Si were observed. These results demonstrate that adsorption products were formed on the surface of the spent SSA/MCM–41. Next, by utilizing the series of extraction and purification operations described in Section 3.5, two white amorphous solids were separated out from the spent SSA/MCM–41, indicating that the anisole was transformed into two adsorption products (I and II) during the reactive adsorption. The results of FTIR and ^{1}H/^{13}C NMR characterization of the adsorption products I and II are shown in Figures S2–S7. In addition, the spectral data of the adsorption products are summarized in Table 4. Based on the above results, we can deduce that the adsorption product I was 4-methoxybenzenesulfonic acid and that product II was 1-methoxy-4-(4-methoxyphenyl)sulfonylbenzene. The schematic reactions for describing the removal mechanism of anisole on SSA/MCM–41 are depicted in Figure 4. This removal process occurred at the gas–solid interface and involved the conversion from anisole to two derivatives (I and II), which could be strongly adsorbed onto the MCM–41 surface due to the higher molecular weights and polarities.

Table 4. ^{1}H/^{13}C NMR and FTIR results of adsorbed products I and II.

Products	Methods and Parameters	The Data of Adsorbed Products
I	^{1}H NMR (DMF, 500 MHz), δ ppm	7.84 (d, J = 5.0 Hz, 2H), 7.11 (d, J = 2.5 Hz, 2H), 3.82 (s, 3H)
	^{13}C NMR (DMF, 125 MHz), δ ppm	56.24, 115.32 (2C), 129.74 (2C), 134.00, 163.33
	FTIR (KBr), cm^{-1}	3427, 2961, 2874, 1610, 1471, 1413, 1235, 1186, 1052, 1014, 840, 768, 677, 576
II	^{1}H NMR (DMF, 500 MHz), δ ppm	7.85 (d, J = 5.0 Hz, 2H), 6.95 (d, J = 5.0 Hz, 2H), 3.84 (s, 3H),
	^{13}C NMR (DMF, 125 MHz), δ ppm	55.62 (2C), 114.44 (4C), 129.55 (4C), 133.84 (2C), 163.14 (2C)
	FTIR (KBr), cm^{-1}	3437, 2926, 2854, 1600, 1495, 1263, 1186, 1148, 1095, 1033, 836, 692, 630, 566
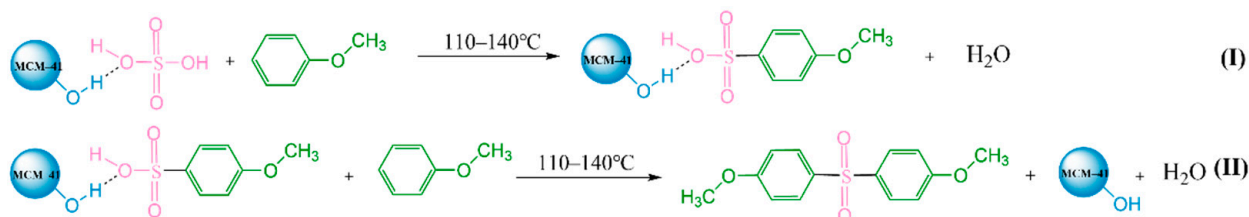
Figure 4. Adsorption reaction of anisole with SSA/MCM–41.

2.4. Reusability of the Supports

The support MCM–41 was readily recovered by solvent extraction of the adsorption products, and it was reused to prepare a recyclable SSA/MCM–41 adsorbent. Figure 5 shows the experimental results for anisole removal by the recyclable SSA/MCM–41. As can be seen, there was no significant loss of Q_B over the five adsorption/desorption cycles, demonstrating good reusability of the MCM–41 as a support.
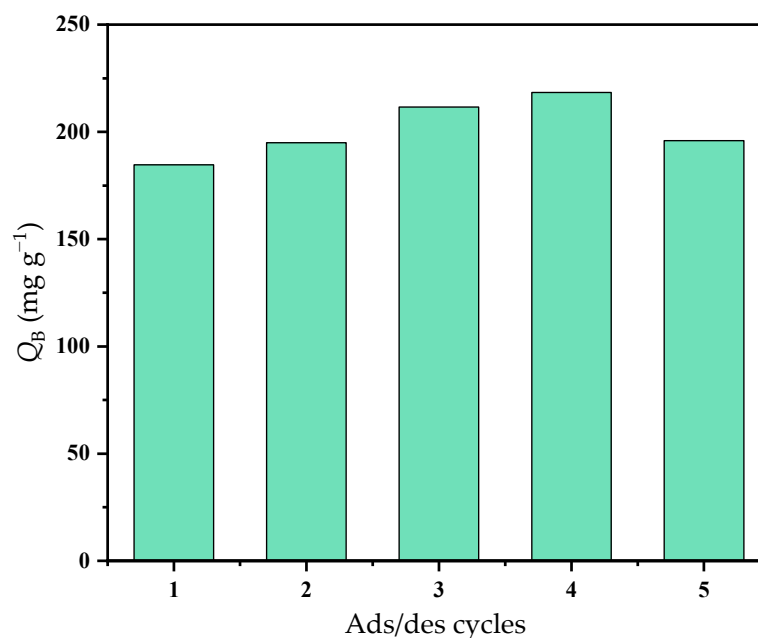

Figure 5. Reusability of SSA/MCM–41 in the cyclic experiments.

3. Experimental Methods

3.1. Materials

The MCM–41 (28–60 nm) used in this study was supplied by Nanjing Nanotechnology Co., Ltd., Nanjing, China. Anisole (>99%, A.R.) was purchased from Yien Chemical Technology Co., Ltd. (Shanghai, China), which was used as the adsorbate gas for adsorption. Sulfuric acid (98%, A.R.) was obtained from Pharmaceutical Chemical Co., Ltd. (Tianjin, China).

3.2. Preparation of Supported Sulfuric Acid

The SSA/MCM–41 catalyst was synthesized by a typical wet impregnation procedure. A sulfuric acid solution (3.7 mL, 5 mol L^{-1}) was mixed with MCM–41 powder (2 g, 0.15 mm), impregnated at ambient conditions for 1 h, and dried in an oven at 80 °C for 48 h. Finally, the catalyst obtained with a sulfuric acid loading of 9.25 mmol g^{-1} was stored in a vacuum desiccator until further use [17,19].

3.3. Characterization

The spent SSA/MCM–41 before and after desorption was characterized by the following techniques: scanning electron microscope (SEM, Hitachi S–4800, Tokyo, Japan) and X-ray energy dispersive spectrometer (EDS, Hitachi, Tokyo, Japan) were used to access the morphology and chemical composition; the chemical structure of the adsorbed products was characterized by Fourier transform infrared spectra (FTIR, Bruker AXS TENSOR 27, Brucker, Germany); proton nuclear magnetic resonance spectra (^{1}H NMR) and carbon nuclear magnetic resonance spectra (^{13}C NMR) were recorded on deuterated dimethyl sulfoxide (DMSO–d_6) or deuterated chloroform (CDCl$_3$) on a Bruker Avance 500 MHz instrument, and tetramethylsilane (TMS) was used as an internal standard.

3.4. Reactive Adsorption Tests

Reactive adsorption tests for removing anisole were conducted in a continuous flow quartz column (6 mm i.d. × 40 cm length) under the following conditions: 50 mg of SSA/MCM–41 catalyst (80–100 mesh) was diluted with 100 mg of quartz sand (80–100 mesh); these materials were then placed into the quartz tube and filled with quartz wool at both ends of the adsorption bed. The anisole gas diluted with N_2 flowed past the sample bed, and its concentration was monitored in real time by GC7900 gas chromatography (Tianmei, China) using a polyethylene glycol (PEG) –20 M capillary column (30 m × 0.32 mm i.d., 0.5 µm film thickness) with a flame ionization detector (FID).

The optimum adsorption bed temperature was determined by the curve of the relationship between the anisole removal rate (X_a) and temperature. The adsorption performance of SSA/MCM–41 was evaluated by measuring the breakthrough time (t_B, min) and breakthrough adsorption capacity (Q_B, mg g^{-1}) under different conditions using control variables (see Table 2) to vary the gas flow rate (V_g, mL min^{-1}), bed height (h, mm), and inlet concentration (C_{in}, mg L^{-1}) of the anisole. Here, t_B was considered the time when the ratio $C_{out,t}/C_{in}$ = 0.05, and X_a and Q_B were derived by Equations (1) and (2) below, respectively:

$$X_a = \frac{C_{in} - C_{out,t}}{C_{in}} \times 100\% \tag{1}$$

$$Q_B = \frac{V_g C_{in}}{m} \int_0^{t_B} \left(1 - \frac{C_{out,t}}{C_{in}}\right) dt \tag{2}$$

where $C_{out,t}$ (mg L^{-1}) is the outlet concentration of anisole in the gas flow, and V_g, h, t_B, Q_B, X_a, and C_{in} are the same as above.

The experimental data were simulated using a dose–response model to better analyze the dynamic adsorption behavior of anisole in the SSA/MCM–41 fixed-bed column and to calculate the theoretical breakthrough time ($t_{B,th}$, min) and theoretical breakthrough adsorption capacity ($Q_{B,th}$, mg g^{-1}) using Equation (3):

$$\frac{C_{out,t}}{C_{in}} = 1 - \frac{1}{1 + \left(\frac{C_{in} \times v \times t}{q_0 \times m}\right)^a} \tag{3}$$

where q_0 and a are constants of the dose–response model.

3.5. Desorption and Regeneration of the Spent SSA/MCM–41

In a previous study, we established a method for adsorbent regeneration and extraction of the adsorbed products [17]. Firstly, the SSA/MCM–41 samples after exposure to anisole were extracted multiple times with absolute ethanol, and the solid residues were repeatedly washed with deionized water and dried at 105 °C to recover the MCM–41. Subsequently, the SSA/MCM–41 was again synthesized using the recovered MCM–41 following the wet impregnation method described above. Next, ethanol extract was concentrated using a rotary evaporator to obtain the adsorbed product. After that, it was dissolved in a small amount of water, then repeatedly extracted with ethyl acetate. Finally, the organic phase was dried using anhydrous Na_2SO_4, filtered, concentrated, and recrystallized from petroleum ether and ethyl acetate (v:v = 2:1) to attain the product.

4. Conclusions

The SSA/MCM–41 material with a H_2SO_4 loading of 9.25 mmol g^{-1} was prepared by the wet impregnation approach and explored as an adsorbent for treating anisole waste gas. The results of the temperature response tests demonstrate that the SSA/MCM–41 adsorbent possessed a 110–140 °C reactive temperature range for anisole, in which X_a was greater than 95%. The results indicated that the dose–response model described the breakthrough adsorption data well. Comprehensive analysis of the process conditions revealed that reducing the flow rate enhanced the anisole removal performances in both $t_{B,th}$ and $Q_{B,th}$,

whereas reducing the inlet concentration or raising the bed height resulted in a trend of first increasing and then slightly decreasing the $Q_{B,th}$ but prolonged the $t_{B,th}$. As a result, the highest $t_{B,th}$ and $Q_{B,th}$ for anisole adsorption on SSA/MCM–41 were determined to be 73.82 min and 247.56 mg g^{-1}, respectively. Furthermore, the FTIR and ^{1}H/^{13}C NMR results reveal that the adsorbed products were 4-methoxybenzenesulfonic acid and 1-methoxy-4-(4-methoxyphenyl)sulfonylbenzene. In conclusion, the anisole removal from the gaseous stream by SSA/MCM–41 followed a reactive adsorption mechanism, which combined the adsorption with sulfonation reactions between the anisole and the anchored H$_2$SO$_4$. In addition, the spent SSA/MCM–41 had good repeatability.

Supplementary Materials: The following are available online at https://www.mdpi.com/article/10.3390/catal12090942/s1: Figure S1, SEM images and EDS spectra of the spent SSA/MCM–41 before (a,b) and after (c,d) desorption; Figure S2, FTIR spectrum of the reactive adsorption product I; Figure S3, FTIR spectrum of the reactive adsorption product II; Figure S4, ^{1}H NMR spectrum of the reactive adsorption product I; Figure S5, ^{13}C NMR spectrum of the reactive adsorption product I; Figure S6, ^{1}H NMR spectrum of the reactive adsorption product II; Figure S7, ^{13}C NMR spectrum of the reactive adsorption product II. Note: In the experiments, product I was 4-methoxybenzenesulfonic acid, and product II was 1-methoxy-4-(4-methoxyphenyl)sulfonylbenzene.

References

1. Zhao, Q.; Li, Y.; Chai, X.; Xu, L.; Zhang, L.; Ning, P.; Huang, J.; Tian, S. Interaction of inhalable volatile organic compounds and pulmonary surfactant: Potential hazards of VOCs exposure to lung. *J. Hazard. Mater.* **2019**, *369*, 512–520. [CrossRef]
2. Xing, Y.; Zhang, W.; Su, W.; Zhang, H.; Wang, J.; Zhang, H.; Guo, Z.; Jia, H. The bibliometric analysis and review of the application of plasma in the field of VOCs. *Catalysts* **2022**, *12*, 173. [CrossRef]
3. He, C.; Cheng, J.; Zhang, X.; Douthwaite, M.; Pattisson, S.; Hao, Z. Recent advances in the catalytic oxidation of volatile organic compounds: A review based on pollutant sorts and sources. *Chem. Rev.* **2019**, *119*, 4471–4568. [CrossRef] [PubMed]
4. Kim, H.S.; Kim, H.J.; Kim, J.H.; Kim, J.H.; Kang, S.H.; Ryu, J.H.; Park, N.K.; Yun, D.S.; Bae, J.W. Noble-metal-based catalytic oxidation technology trends for volatile organic compound (VOC) removal. *Catalysts* **2022**, *12*, 63. [CrossRef]
5. Ma, X.; Zhao, D.; Qian, J.; Ma, Z.; Cui, J. Utilization of hematite particles for economical removal of *o*-xylene in a high-temperature gas-solid reactor. *Molecules* **2022**, *27*, 1509. [CrossRef] [PubMed]
6. Yue, X.; Ma, N.L.; Sonne, C.; Guan, R.; Lam, S.S.; Van Le, Q.; Chen, X.; Yang, Y.; Gu, H.; Rinklebe, J.; et al. Mitigation of indoor air pollution: A review of recent advances in adsorption materials and catalytic oxidation. *J. Hazard. Mater.* **2021**, *405*, 124138. [CrossRef]
7. Rochard, G.; Olivet, L.; Tannous, M.; Poupin, C.; Siffert, S.; Cousin, R. Recent advances in the catalytic treatment of volatile organic compounds: A review based on the mixture effect. *Catalysts* **2021**, *11*, 1218. [CrossRef]
8. Zhan, J.; Feng, Z.; Liu, P.; He, X.; He, Z.; Chen, T.; Wang, Y.; He, H.; Mu, Y.; Liu, Y. Ozone and SOA formation potential based on photochemical loss of VOCs during the Beijing summer. *Environ. Pollut.* **2021**, *285*, 117444. [CrossRef]
9. Zhu, L.; Shen, D.; Luo, K.H. A critical review on VOCs adsorption by different porous materials: Species, mechanisms and modification methods. *J. Hazard. Mater.* **2020**, *389*, 122102. [CrossRef]
10. Veerapandian, S.K.P.; De Geyter, N.; Giraudon, J.M.; Lamonier, J.F.; Morent, R. The use of zeolites for VOCs abatement by combining non-thermal plasma, adsorption, and/or catalysis: A review. *Catalysts* **2019**, *9*, 98. [CrossRef]
11. Mamaghani, A.H.; Haghighat, F.; Lee, C.S. Photocatalytic oxidation technology for indoor environment air purification: The state-of-the-art. *Appl. Catal. B* **2017**, *203*, 247–269. [CrossRef]

12. Warahena, A.S.; Chuah, Y.K. Energy recovery efficiency and cost analysis of VOC thermal oxidation pollution control technology. *Environ. Sci. Technol.* **2009**, *43*, 6101–6105. [CrossRef] [PubMed]

13. Baskaran, D.; Sinharoy, A.; Pakshirajan, K.; Rajamanickam, R. Gas-phase trichloroethylene removal by rhodococcus opacus using an airlift bioreactor and its modeling by artificial neural network. *Chemosphere* **2020**, *247*, 125806. [CrossRef] [PubMed]

14. Guo, Y.; Wen, M.; Li, G.; An, T. Recent advances in VOC elimination by catalytic oxidation technology onto various nanoparticles catalysts: A critical review. *Appl. Catal. B* **2021**, *281*, 11947. [CrossRef]

15. Wu, P.; Jin, X.; Qiu, Y.; Ye, D. Recent progress of thermocatalytic and photo/thermocatalytic oxidation for VOCs purification over manganese-based oxide catalysts. *Environ. Sci. Technol.* **2021**, *55*, 4268–4286. [CrossRef]

16. Dong, Y.; Liu, Y.; Wang, J.; Gao, K.; Ma, Z. Silica supported sulfuric acid for the removal of gaseous *o*-xylene. *J. Environ. Chem. Eng.* **2019**, *7*, 102992. [CrossRef]

17. Gao, K.; Ma, M.; Liu, Y.; Ma, Z. A comparative study of the removal of *o*-xylene from gas streams using mesoporous silicas and their silica supported sulfuric acids. *J. Hazard. Mater.* **2021**, *409*, 124965. [CrossRef]

18. Zhao, D.; Ma, M.; Qian, J.; Wang, Y.; Ma, Z.; Ma, X. Influence of impregnation medium on the adsorptive performance of silica sulfuric acid for the removal of gaseous *o*-xylene: Comparison on ethyl acetate and water. *Catalysts* **2022**, *12*, 737. [CrossRef]

19. Ma, M.; Gao, K.; Ma, Z.; Ding, J. Influence of preparation method on the adsorptive performance of silica sulfuric acid for the removal of gaseous *o*-xylene. *Sep. Purif. Technol.* **2021**, *265*, 118484. [CrossRef]

20. El-Hakam, S.A.; Alshorifi, F.T.; Salama, R.S.; Gamal, S.; El-Yazeed, W.S.A.; Ibrahim, A.A.; Ahmed, A.I. Application of nanostructured mesoporous silica/bismuth vanadate composite catalysts for the degradation of methylene blue and brilliant green. *J. Mater. Res. Technol.* **2022**, *18*, 1963–1976. [CrossRef]

21. Salama, R.S.; El-Bahy, S.M.; Mannaa, M.A. Sulfamic acid supported on mesoporous MCM-41 as a novel, efficient and reusable heterogenous solid acid catalyst for synthesis of xanthene, dihydropyrimidinone and coumarin derivatives. *Colloids Surf. A Physicochem. Eng. Asp.* **2021**, *628*, 127261. [CrossRef]

22. Ibrahim, A.A.; Salama, R.S.; El-Hakam, S.A.; Khder, A.S.; Ahmed, A.I. Synthesis of 12-tungstophosphoric acid supported on Zr/MCM-41 composite with excellent heterogeneous catalyst and promising adsorbent of methylene blue. *Colloids Surf. A Physicochem. Eng. Asp.* **2021**, *631*, 127753. [CrossRef]

23. Yang, X.; Liu, Y.B. Anisole is an environmentally friendly fumigant for postharvest pest control. *J. Stored Prod. Res.* **2021**, *93*, 101842. [CrossRef]

24. Chen, J.; Sun, C.; Huang, Z.; Qin, F.; Xu, H.; Shen, W. Fabrication of functionalized porous silica nanocapsules with a hollow structure for high performance of toluene adsorption-desorption. *ACS Omega* **2020**, *5*, 5805–5814. [CrossRef]

25. Laskar, I.I.; Hashisho, Z.; Phillips, J.H.; Anderson, J.E.; Nichols, M. Modeling the effect of relative humidity on adsorption dynamics of volatile organic compound onto activated carbon. *Environ. Sci. Technol.* **2019**, *53*, 2647–2659. [CrossRef]

26. Wang, J.; Cao, S.; Sun, Y.; Meng, X.; Wei, J.; Ge, Y.; Liu, B.; Gong, Y.; Li, Z.; Mo, G. β Zeolite nanostructures with a high SiO_2/Al_2O_3 ratio for the adsorption of volatile organic compounds. *ACS Appl. Nano Mater.* **2021**, *4*, 13257–13266. [CrossRef]

27. Calero, M.; Hernainz, F.; Blazquez, G.; Tenorio, G.; Martin-Lara, M.A. Study of Cr (III) biosorption in a fixed-bed column. *J. Hazard. Mater.* **2009**, *171*, 886–893. [CrossRef]

28. Fakhfakh, N.; Dammak, N.; Benzina, M. Breakthrough modeling and experimental design for *o*-xylene dynamic adsorption onto clay material. *Environ. Sci. Pollut. Res. Int.* **2018**, *25*, 18263–18277. [CrossRef]

29. Ma, M.; Gao, K.; Zhao, D.; Ma, X.; Ma, Z. Effect of process conditions on reaction-type adsorption of *o*-xylene by MCM-41 supported sulfuric acid: Model simulations of breakthrough curves. *J. Environ. Chem. Eng.* **2022**, *10*, 106937. [CrossRef]

30. Hong, T.; Wei, L.; Cui, K.; Dong, Y.; Li, R.; Zhang, T.; Zhao, Y.; Luo, L. Adsorption performance of volatile organic compounds on activated carbon fibers in a fixed bed column. *J. Environ. Chem. Eng.* **2021**, *9*, 106347. [CrossRef]